CHEMISTRY OF MATERIALS

Article

pubs.acs.org/cm

Titanium Doping and Its Effect on the Morphology of Three-Dimensional Hierarchical $Nb_3O_7(OH)$ Nanostructures for Enhanced Light-Induced Water Splitting

Sophia B. Betzler,[†,‡] Filip Podjaski,[§,¶] Michael Beetz,[†] Kathrin Handloser,[†,‡] Andreas Wisnet,[†,‡] Matthias Handloser,[†,‡] Achim Hartschuh,[†,‡] Bettina V. Lotsch,[†,‡,§] and Christina Scheu*[,∥]

[†]Department of Chemistry and Center for NanoScience, Ludwig-Maximilians-Universität, Butenandtstraße 11, 81377 Munich, Germany

[‡]Nanosystems Initiative Munich, Schellingstraße 4, 80799 Munich, Germany

[§]Max-Planck-Institut für Festkörperforschung, Heisenbergstraße 1, 70569 Stuttgart, Germany

[∥]Max-Planck-Institut für Eisenforschung GmbH, Max-Planck-Straße 1, 40237 Düsseldorf, Germany

[¶]Ecole Polytechnique Féderale de Lausanne, Station 12, CH-1015 Lausanne, Switzerland

Supporting Information

ABSTRACT: This study presents a simple method that allows us to modify the composition, morphological, and surface properties of three-dimensional hierarchical $Nb_3O_7(OH)$ superstructures, resulting in strongly enhanced photocatalytic H_2 production. The superstructures consist of highly ordered nanowire networks and self-assemble under hydrothermal conditions. The presence of titanium affects the morphology of the superstructures, resulting in increased surface areas for higher doping levels. Up to 12 at. % titanium is incorporated into the $Nb_3O_7(OH)$ crystal lattice via substitution of niobium at its octahedral lattice sites. Further titanium excess results in the formation of niobium-doped TiO_2 plates, which overgrow the surface of the $Nb_3O_7(OH)$ superstructures. Photoluminescence spectroscopy indicates fewer charge recombination processes near the surface of the nanostructures with an increasing titanium concentration in the crystal lattice. The combination of larger surface areas with fewer quenching sites at the crystal surface yields higher H_2 evolution rates for the doped samples, with the rate being doubled by incorporation of 5.5 ± 0.7 at. % Ti.

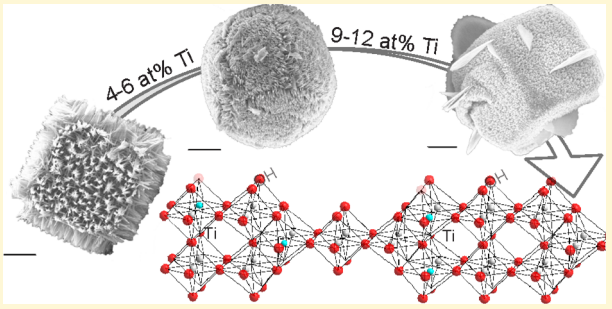

INTRODUCTION

Hydrogen is a key fuel not only for the chemical industry but also as a suitable energy source of the future.[1] Photocatalytic water splitting is an environmentally friendly approach for hydrogen production that mimics natural photosynthesis using solar energy to convert water into hydrogen and oxygen gas. The endergonic reaction is enabled by a semiconductor: an absorbed photon excites an electron from the valence to the conduction band creating an electron−hole pair. If the potential of this electron−hole pair is sufficient, the electron reduces and the hole oxidizes water to hydrogen and oxygen.[2] The photocatalytic activity of a material generally depends upon several electronic and morphological factors. The size and energetic position of the band gap with respect to the standard hydrogen electrode determines whether the charge transport from the photocatalyst to water can take place (the theoretical minimum band gap for water splitting is 1.23 eV without overpotential).[2] TiO_2 is one of the most intensively studied semiconductors in the field of photochemistry,[3,4] in both the realm of photocatalysis[5−7] and solar cell devices.[8−11] However, the achieved rates are far too low for commercial use,[12] thus enforcing the research of alternative material systems.[13−16] Niobium-based metal oxides attract increasing attention in the field of photocatalysis and also serve as possible candidates for water-splitting applications.[17−28] Similar to TiO_2, their crystal structures are built up from NbO_6 octahedra and their band gaps range from 3.1 eV[29] to 4.9 eV[30] for different modifications. The capability for photocatalytic water splitting could already be shown for Nb_2O_5,[18,23] $Nb_3O_7(OH)$,[25] and several other niobates.[12]

The actual water-splitting redox reaction happens at the surface of the semiconductor, and accordingly, a high surface area is beneficial. The photogenerated electron−hole pair has to diffuse to the surface of the nanostructure, a process threatened by recombination, a major loss mechanism resulting in reduced efficiencies.[31] A low number of defects in the crystal lattice and nanostructures with small dimensions reduce the probability of electron−hole recombination, while large surface

Received: June 27, 2016
Revised: October 12, 2016
Published: October 13, 2016

DOI: 10.1021/acs.chemmater.6b02470
Chem. Mater. 2016, 28, 7666−7672

areas increase the number of active reaction sites.[2] Thus, crystalline morphologies consisting of small nanostructures are expected to show the highest turnover rates. In the following, we describe hierarchically ordered nanostructures as superstructures. As reported previously by our group, three-dimensional (3D) hierarchical $Nb_3O_7(OH)$ superstructures can be synthesized using a template-free one-step hydrothermal synthesis approach. The superstructures are composed of nanowire networks and benefit from a large surface area combined with a high crystallinity of the one-dimensional crystals.[24] This study presents a facile strategy that allows us to rationally modify the morphology and water-splitting capability of these $Nb_3O_7(OH)$ superstructures via the addition of Ti(IV) to the reaction solution. The presence of Ti(IV) causes decreased nanowire sizes and altered morphologies. The dependence of the morphology and crystallographic properties of $Nb_3O_7(OH)$ superstructures and their building blocks on the Ti(IV) concentration was investigated in detail using electron microscopy and X-ray diffraction (XRD) experiments. The results are correlated with the material properties and hydrogen production rate, which increases drastically with the Ti(IV) concentration.

RESULTS AND DISCUSSION

Effect of the Incorporation of Titanium on the Morphology and Crystal Structure. Undoped $Nb_3O_7(OH)$ superstructures, which grow under hydrothermal conditions at 200 °C, form the starting point of this study. The orthorhombic crystal structure of $Nb_3O_7(OH)$ is composed of blocks of corner-sharing NbO_6 octahedra. The walls of the hollow, cubic superstructures consist of nanowire networks. Additional nanowires, which point like spikes from their surfaces, further enhance the surface area of the superstructures (Figure 1a).[24] This morphology is named morphology A in the following. Energy-dispersive X-ray (EDX) spectroscopy shows a linear dependence between the Ti amount incorporated into the superstructures, given relative to Nb, and the Ti(IV) concentration in the reaction solution (see Figures S1 and S2 of the Supporting Information). The addition of small Ti(IV) concentrations between 0.03 and 0.06 mol L^{-1} causes the formation of a spherical morphology with an average amount of 5.5 ± 0.7 at. % titanium incorporated into the crystal lattice of $Nb_3O_7(OH)$ (morphology B). These results are furthermore confirmed by inductively coupled plasma mass spectrometry, which yields a Nb amount of 766.60 ± 8.55 mg g^{-1} (8.25 ± 0.09 mmol g^{-1}) and a Ti amount of 23.38 ± 2.46 mg g^{-1} (0.49 ± 0.05 mmol/g^{-1}) (see Table S1 of the Supporting Information). Morphology B is likewise hollow and built up from nanowires (Figure 1b and Figure S3 of the Supporting Information). Scanning electron microscopy (SEM) images reveal sutures on its surface, which might be remainings of former cube edges, and propose that the spheres are rounded cubes (see Figure S4 of the Supporting Information). The XRD pattern of these samples matches the diffraction pattern detected for undoped, phase-pure $Nb_3O_7(OH)$ superstructures. With an increasing titanium concentration in the reaction solution (0.09−0.11 mol L^{-1}), a cubic morphology forms (morphology C). In contrast to the cubes found in the absence of Ti(IV), these cubes consist of noticeably smaller nanowires, which arrange to form the walls of hollow cubes (Figure 1c). For this sample, the XRD pattern reveals a phase mixture and reflections of the anatase TiO_2 phase are visible in addition to the reflections of $Nb_3O_7(OH)$. They can be attributed to the formation of large TiO_2 plates on the surface of some of the cubes, as visible in SEM micrographs. EDX measurements in the SEM yield a Ti content of 10.8 ± 1.5 at. % for morphology C, which is not overgrown by large plates, and a significantly higher Ti content of 31.2 ± 5.0 at. % for morphology C overgrown by TiO_2 plates. Thus, two effects are observed: First, the incorporation of titanium yields smaller wire dimensions with the amount of titanium, which can be incorporated into the $Nb_3O_7(OH)$ crystal lattice being limited. Second, titanium excess leads to the formation of an additional TiO_2 phase.

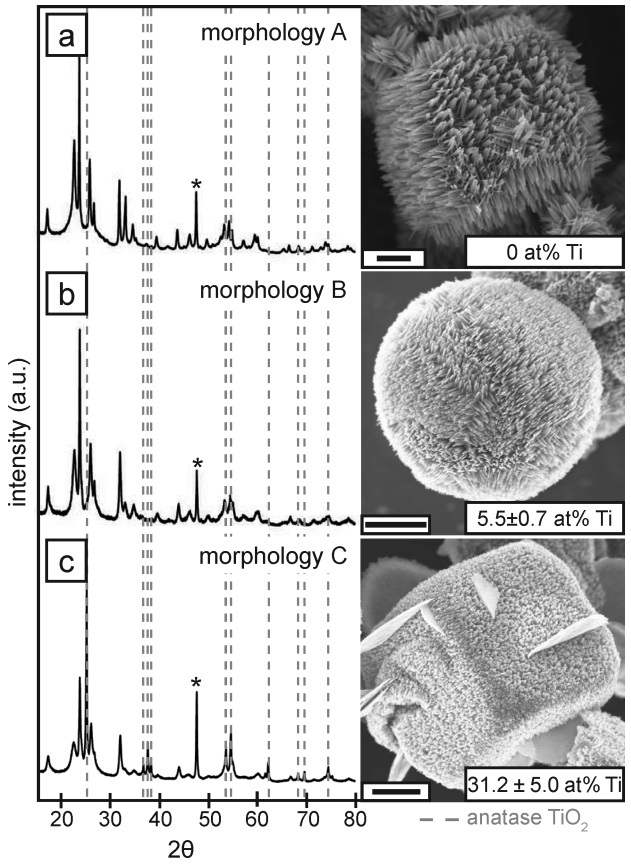

Figure 1. Morphology and crystal structure of $Nb_3O_7(OH)$ superstructures, which form for different Ti(IV) concentrations in the reaction solution. On the right side, SEM images of morphologies A, B, and C are displayed (scale bar of 1 μm), with the titanium content averaged over the morphology indicated relative to niobium. (a−c) Left side shows XRD patterns of the respective samples. The gray dashed lines highlight the reflections belonging to the anatase TiO_2 crystal phase [Inorganic Crystal Structure Database (ICSD), Card 44882]; all others are caused by $Nb_3O_7(OH)$ {isomorphous to Nb_3O_7F[32] [Joint Committee on Powder Diffraction Standards (JCPDS), Card 74-2363]}. A reflection caused by the instrumental setup is marked by an asterisk. The *d* values are listed in Table S2 of the Supporting Information.

The XRD pattern shows a shifting of the reflections depending on the titanium amount incorporated into the crystal lattice. With an increasing Ti concentration in the crystal lattice, the different diffraction orders of the (100) planes shift to larger angles, signifying a decreased *d* spacing. In contrast, the (001) reflection shifts to smaller angles, related to an expansion of the *c*-lattice parameter (see Figure S5 and Table S3 of the Supporting Information). The expansion of the crystal lattice indicates the incorporation of point defects.[33] The replacement of Nb^{5+} by Ti^{4+} necessitates the removal of anions

DOI: 10.1021/acs.chemmater.6b02470
Chem. Mater. 2016, 28, 7666−7672

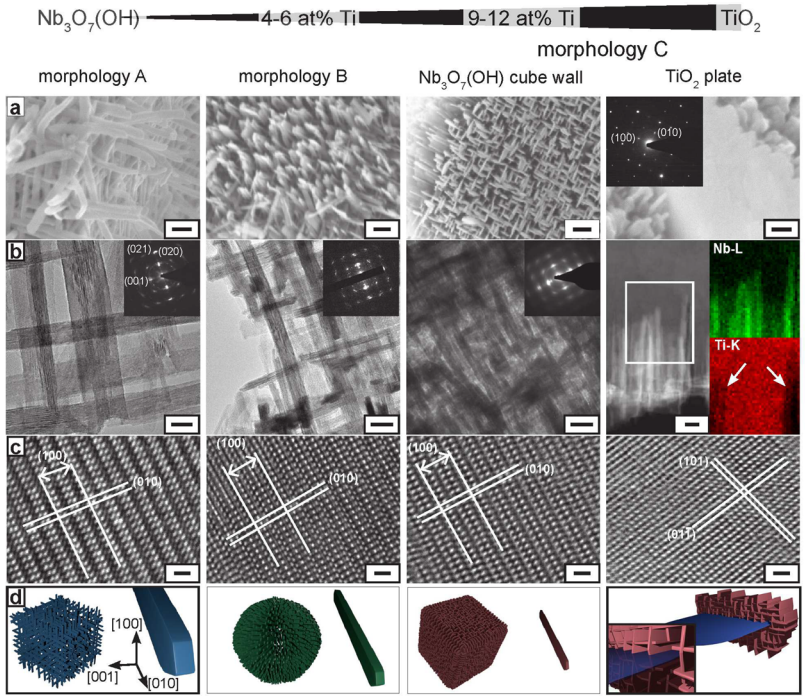

Figure 2. Electron microscopy analysis of the superstructures achieved for different Ti(IV) concentrations in the reaction solution. The amount of titanium incorporated into the crystal lattice increases from left to right. SEM images of the different morphologies and the TiO_2 plates are displayed in panel a (scale bar of 100 nm). (b) TEM images of fragments of the nanowire networks building up the walls of the different morphologies (scale bar of 20 nm). The inset shows the diffraction pattern of the respective network observed in the [100] direction (scale bar of 20 nm). For the TiO_2 plate, a scanning TEM image of the conduit region between the cube wall and plate is given together with EDX maps (Ti−K and Nb−L line) of the highlighted region (scale bar of 20 nm). (c) HRTEM images of a nanowire of each morphology (in the [001] direction) and the TiO_2 plate (in the [$\bar{1}$11] direction) (scale bar of 1 nm). (d) Schematic drawings that illustrate the shape of the building blocks true to scale (see Table S4 of the Supporting Information). For the TiO_2 plate, the connection between the TiO_2 plate and $Nb_3O_7(OH)$ cube wall is displayed.

from the crystal lattice for charge balance. For $Nb_3O_7(OH)$, charge balance is most likely obtained by removing hydroxyl groups from the crystal lattice, yielding $Nb_{3-x}Ti_xO_7(OH)_{1-x}$. XRD analysis shows a reduced lattice parameter in the *a* direction for an increasing titanium concentration. As the crystal ionic radius of 6-fold coordinated Ti(IV) is reported to be 3.5 pm smaller than the radius of 6-fold coordinated Nb(V),[34] the contraction of the crystal lattice in the *a* direction might result from the replacement of Nb(V) by Ti(IV). This and the distribution of titanium in the crystal lattice of $Nb_3O_7(OH)$ are investigated in more detail by transmission electron microscopy (TEM) and will be discussed below.

In-Depth TEM Characterization of the Nanowire Networks. TEM investigations are performed for a deeper understanding of the correlation between the crystal size and titanium incorporation. As reported previously, morphology A consists of highly ordered nanowire networks (Figure 1a), which reflects in both bright field (BF) images and the electron diffraction pattern of the networks (Figure 2b).[24] The nanowires forming the networks grow in the [010] direction and possess larger (001) and slightly smaller (100) crystal facets (true to scale schemes in Figure 2d and Figure S6 and Table S4 of the Supporting Information). The indexing of the electron pattern recorded for the nanowire networks proves that they are a superposition of orthogonally aligned nanowires, which possess the [100] zone axis.[24] In addition to the main reflections, low-intensity reflections appear in the diffraction pattern, which originate from detached nanowires. From BF images, it is obvious that the walls of morphology B consist of the same nanowire arrangement (Figure 2a). However, the nanowires are smaller and shorter and have an altered aspect ratio of the (001) to (100) crystal facets than pristine $Nb_3O_7(OH)$ nanowires (see schematic in Figure 2d). This trend continues, so that the nanowires observed for morphology C are noticeably smaller, shorter, and flatter. This causes a rather compact appearance of the cube wall in BF images and broadened reflections in the corresponding electron diffraction pattern of the cube wall. In addition, the broadening of the reflections also indicates a slight rotation of the building blocks relative to each other. Still, the overall nanowire arrangement is preserved, and the *d* spacing of the reflections matches $Nb_3O_7(OH)$. Local EDX spectra recorded at the nanowire network of morphology C yield a titanium concentration of 11.1 at. % titanium, which is in the range of the titanium amount observed for TiO_2-free cubes of morphology C in the SEM. SEM images reveal large plates on the surface of morphology C (Figures 1c and 2a). Electron diffraction experiments prove that these plates are single-crystalline anatase TiO_2 observed in the [001] direction (Figure 2c), which matches the results of the XRD analysis (Figure 1c). EDX measurements reveal a homogeneous distribution of 23 ± 1 at. % niobium within these plates. Figure 2a shows a SEM image of the conduit region between the cube wall and TiO_2 plate, demonstrating that the TiO_2 plate is connected to the $Nb_3O_7(OH)$ nanowires of the cube wall. The combination of scanning TEM and EDX investigations indicates a disruption of the TiO_2 plate by integrated $Nb_3O_7(OH)$ nanowires, causing a decreased Ti concentration in these regions, visible in EDX maps of the Ti−K line (marked with white arrows in Figure 2b). Nanowires lying on top or below the TiO_2 plate, which are

DOI: 10.1021/acs.chemmater.6b02470
Chem. Mater. 2016, 28, 7666−7672

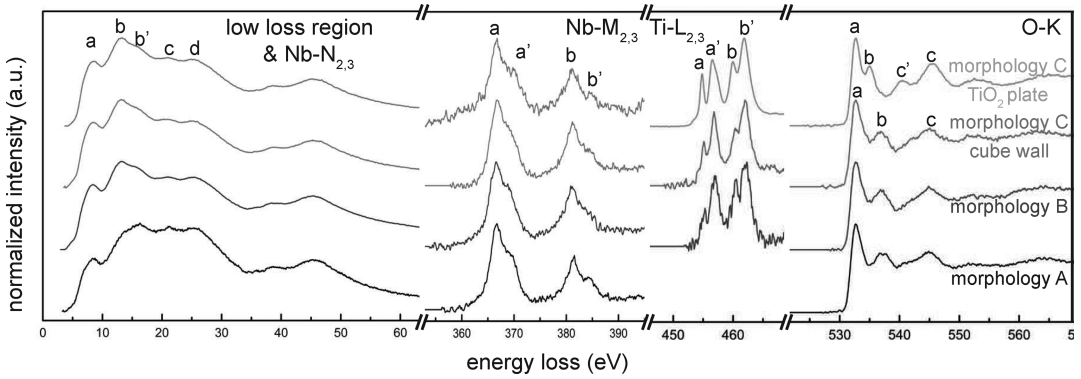

Figure 3. EELS detected for morphologies A and B and the wall of the cubes and TiO_2 plate of morphology C. The low loss region and ELNES of the Nb−$N_{2,3}$, Nb−$M_{2,3}$, Ti−$L_{2,3}$, and O−K edges are displayed, with significant features marked with letters a−d referred to in the text.

visible in the Nb EDX map, on the contrary, do not cause a strongly modified contrast in the Ti EDX maps. In this regard, morphology C can actually be regarded as a composition of two morphologies: the $Nb_3O_7(OH)$ cubes form the basis, which is partly overgrown by anatase TiO_2 plates.

It is important to find out if titanium is distributed homogeneously in the $Nb_3O_7(OH)$ lattice or enriched in certain areas. Hydrothermally grown $Nb_3O_7(OH)$ nanowires are characterized by planar defects parallel to the {001} lattice planes. These defects have a homogeneous width, which apparently does not change as a result of the incorporation of titanium into the crystal lattice (see Figure S7 of the Supporting Information). Figure 2c shows high-resolution transmission electron microscopy (HRTEM) images detected in the [001] direction, which do not indicate significant changes of the $Nb_3O_7(OH)$ crystal lattice as a result of the presence of titanium (Figure 2c). These results are confirmed by EDX maps, which indicate a homogeneous distribution of titanium throughout the nanowires, and no areas of higher Ti concentration are observed, including nanowire junctions (see Figure S8 of the Supporting Information). Together with the XRD analysis, these results prove the homogeneous distribution of titanium in the crystal lattice of $Nb_3O_7(OH)$, while an accumulation of titanium at grain boundaries or defects cannot be observed within the detection limit of our measurements. The incorporation of titanium as a dopant in the crystal lattice of $Nb_3O_7(OH)$ results in altered crystal sizes and shapes, which lead to different morphologies at the microscale. In addition, the findings suggest that the crystal lattice of $Nb_3O_7(OH)$ is not capable of accommodating more than about 12 at. % Ti, so that the formation of niobium-doped anatase TiO_2 is favored for further titanium excess. HRTEM images detected at the conduit region of the $Nb_3O_7(OH)$ nanoplate and TiO_2 plate show that this happens via oriented crystal growth (see Figure S9 of the Supporting Information).

Electron Energy-Loss Spectroscopy Study of Titanium-Doped Samples. For a better understanding of the local surrounding of doped titanium atoms in the $Nb_3O_7(OH)$ lattice, electron energy-loss spectroscopy (EELS) was performed. The energy-loss near-edge fine structure (ELNES) of the Ti−$L_{2,3}$, Nb−$M_{2,3}$, and O−K edges is analyzed for morphologies A and B and for both the cube wall and TiO_2 plate of morphology C (Figure 3 and Table S5 of the Supporting Information). The features in the low loss regime are dominated by plasmon excitations and have a similar shape for all samples. Only the intensity ratio of peak b and b′ varies, and the decreased intensity of feature b observed for morphology A could either result from the absence of titanium in the crystal lattice or be caused by different sample thicknesses.

The Nb−$M_{2,3}$ and Ti−$L_{2,3}$ edges result from the excitation of Nb 3p and Ti 2p electrons to unoccupied Nb 4d or Ti 3d states. The shape of these two edges is characterized by two white lines, which reflect the spin−orbital splitting of the 3p orbitals of niobium and 2p orbitals of titanium. The splitting of the Nb−$M_{2,3}$ white lines (peaks a and b) is identical for all investigated samples. Additional high-energy shoulders (a′ and b′) appear for both the Nb−M_3 and Nb−M_2 edges of all samples, indicating the presence of pentavalent niobium.[35] The Ti−L_3 and Ti−L_2 white lines (peaks a and b) are further split up to form doublets (additional peaks a′ and b′) for morphology B and both the cube wall and TiO_2 plate of morphology C. This splitting is due to unoccupied t_{2g} levels, which hints at the presence of Ti(IV) in the $Nb_3O_7(OH)$ crystal lattice.[36,37] This assumption is strengthened by the measured peak splitting of peaks a and b, which is 5.2 ± 0.1 eV for the three samples. This value fits the literature value of both rutile and anatase TiO_2 (5.4 eV[36]). The ELNES of the Ti−$L_{2,3}$ edge detected for the TiO_2 plate of morphology C shows an additional high-energy shoulder for peak a′ (see Figure S10 of the Supporting Information). This feature is characteristic for anatase TiO_2 and originates from the distortion of the TiO_6 octahedra in the crystal lattice.[37] The ELNES of the O−K edge of morphology A is dominated by three distinct peaks (a, b, and c) with intensities and energy splitting matching those reported for Nb_2O_5.[35] Neither the intensity nor the splitting of the peaks is strongly affected by the incorporation of titanium in the crystal lattice. However, significant differences are observed for the ELNES of the TiO_2 plate of morphology C, which shows a drastically decreased splitting of peaks a and b and the appearance of an additional peak c′. The shape and peak splitting of this O−K ELNES match anatase TiO_2.[36,37]

The ELNES of the Ti−$L_{2,3}$, Nb−$M_{2,3}$, and O−K edges does not show significant changes as a result of the incorporation of titanium into the crystal lattice of $Nb_3O_7(OH)$. The unit cell of $Nb_3O_7(OH)$ is composed of NbO_6 octahedra. The shape of the Ti−$L_{2,3}$ edge resembles the ELNES of anatase and rutile TiO_2;[36] both crystal structures consist of TiO_6 octahedra. The ELNES of the Ti−$L_{2,3}$ edge, together with the fact that neither the shape of the O−K nor the Nb−$M_{2,3}$ edge is affected by incorporated titanium, indicates the replacement of niobium by titanium at its octahedral lattice sites. In the case of the TiO_2

DOI: 10.1021/acs.chemmater.6b02470
Chem. Mater. 2016, 28, 7666−7672

plate, the ELNES of both the O−K and Ti−$L_{2,3}$ edges confirms the results of the diffraction experiments. The TiO_2 plate incorporates niobium, and the shape of the Nb−$M_{2,3}$ edge indicates the presence of octahedrally coordinated pentavalent niobium, suggesting the replacement of titanium by niobium.

Photocatalytic Activity of the Different Morphologies. As expected from the SEM images, Brunauer−Emmett−Teller (BET) measurements confirm the high surface area of the different morphologies, yielding 79 $m^2\ g^{-1}$ for morphology A, 132 $m^2\ g^{-1}$ for morphology B, and 173 $m^2\ g^{-1}$ for morphology C. Morphologies A and B show similar extinction spectra with a strong absorbance below 390 nm, which fits the band gap of 3.2 eV reported for $Nb_3O_7(OH)$.[24,29] For morphology C, the same band gap was measured but an additional slightly enhanced absorbance in the red spectral region (550−850 nm) is observed. This is most likely related to the presence of oxygen vacancies in the TiO_2 plates (see Figure S11 of the Supporting Information).[38] Previous studies show the photocatalytic activity of pristine $Nb_3O_7(OH)$[24,29] and also its photocatalytic stability.[26] However, a recent study proposes that proton reduction is kinetically hindered on the surface of $Nb_3O_7(OH)$ as in most oxides.[25] Therefore, in the present work, the hydrogen production rate is measured on Pt-decorated 3D hierarchical $Nb_3O_7(OH)$ superstructures. The Pt decoration is achieved by chloroplatinic acid treatment, and TEM investigations show homogeneous particle distribution for the different samples. Statistical analysis reveals an average particle diameter of 3.6 nm for morphology A, an average particle diameter of 2.5 nm for morphology B, and an average particle diameter of 3.3 nm for morphology C, but the overall particle density appears similar (see Figure S12 of the Supporting Information). Hence, the size variation between the different samples is small, and therefore, its effect on the water-splitting capability is neglected. To account for the size of the band gap and to allow for efficient charge-carrier generation, a 600 mW cm^{-2} xenon lamp, which emits 2.7−1.1 $\mu W\ cm^{-2}\ nm^{-1}$ in the spectral region of 280−390 nm (see Figure S13 of the Supporting Information), is used to measure the hydrogen evolution rate of the different morphologies. Undoped $Nb_3O_7(OH)$ yields a rate of 870 $\mu mol\ g^{-1}\ h^{-1}$, which is similar to the rate reported for Pt-decorated $Nb_3O_7(OH)$ nanowires that do not form a 3D arrangement.[25] This rate increases with increasing Ti concentration, featuring a rate of 1773 $\mu mol\ g^{-1}\ h^{-1}$ for morphology B and 1988 $\mu mol\ g^{-1}\ h^{-1}$ for morphology C (Table 1). The catalytic rates were determined by measuring the evolved hydrogen in 1 h steps for the first 5 h. In addition, some of the samples were measured again after 25 h, and the hydrogen amount produced after this time nicely matches the linear dependency discovered for the shorter time frames, indicating the long-term stability of the material (see Figure S14 of the Supporting Information).

Table 1. H_2 Production Rate, Surface Area, and PL Lifetime for Different $Nb_3O_7(OH)$ Superstructures, which Comprise Different Titanium Amounts

	Ti amount (at. %)	surface area from BET ($m^2\ g^{-1}$)	PL lifetime measured via TCSPC (ps)	H_2 production Xenon lamp 600 mW cm^{-2} ($\mu mol\ g^{-1}\ h^{-1}$)
morphology A	0	79	54 ± 2	870
morphology B	5.5 ± 0.7	132	64 ± 2	1773
morphology C	31.2 ± 5.0	173	73 ± 4	1988

To gain further insight into the effect of Ti doping on the photocatalytic properties of the material, we investigated the photoluminescence (PL) lifetime of the electronic states populated upon optical excitation for the different morphologies (in the absence of platinum) using time-correlated single-photon counting (TCSPC) (Figure 4a). Two-photon excitation at 730 nm (1.7 eV) was provided by a Ti/Sa oscillator at a repetition rate of 76 MHz, and the optical response of the samples was detected for wavelengths shorter than 600 nm. Ultrashort excitation pulses of 150 fs in combination with a fast photodetector and timing electronics (see Figure 15 of the Supporting Information) lead to a temporal resolution of about 3 ps.[39] This technique allows us to detect changes in the excited-state relaxation and helps to distinguish radiative and non-radiative rate modifications. TCSPC transients were recorded at five individual sample spots for each morphology (see Figure S15 of the Supporting Information), and the extracted PL lifetimes are averaged to minimize the influence of material heterogeneities (Figure 4b). All samples showed biexponential decay with time constants of around 6−10 and 150−200 ps for the short and long decay times, respectively. For morphology A, an intensity-averaged lifetime of 54 ± 2 ps is observed. Morphology B features a somewhat longer lifetime of 64 ± 2 ps. For morphology C, an intensity-averaged lifetime of 73 ± 4 ps is recorded.

From Figure 4, it thus becomes evident that, for increasing Ti amounts incorporated into the superstructures, the excited-state lifetime becomes longer. The enhanced PL lifetime for increasing Ti amounts can be attributed to a reduction of non-radiative losses and, with that, to a lower density of quenching sites existing near the crystal surfaces. One possible explanation could be that the replacement of Nb^{5+} by Ti^{4+} decreases the amount of hydroxyl groups required for charge neutrality, featuring a lower hydroxyl concentration in the crystal lattice of doped samples $Nb_{3-x}Ti_xO_7(OH)_{1-x}$. Hydroxyl groups are known for acting as non-radiative recombination sites.[40,41] Therefore, the doubled H_2 production rate of morphology B compared to morphology A is most likely due to a combination of the decreasing amount of recombination sites and larger surface area of morphology B because neither of the two morphologies contains TiO_2. A further increase of the H_2 production rate, but less pronounced, is seen for morphology C, which indicates that the presence of TiO_2 plates observed for this morphology does not have a strong effect on the photocatalytic reaction.

CONCLUSION

This study investigates the effect of titanium doping on the morphology and properties of 3D hierarchical $Nb_3O_7(OH)$ superstructures and their performance as photocatalyst material. The integration of titanium at the octahedral lattice sites of $Nb_3O_7(OH)$ affects its crystallization, leading to reduced growth rates, whereas the growth in the *b* and *c* directions is affected more strongly than the growth in the *a* direction. It seems that the modified shapes of the nanowires or altered surface charges influence the interparticular forces, which drive the organized self-assembly of the superstructures, because the findings of this study yield no evidence for an involvement of TiO_2 islands at nanowire junctions. In the absence of titanium, hollow cubes, which consist of highly ordered nanowire networks, form. For a doping degree of 5.5 ± 0.7 at. % Ti, the formation of hollow spheres constituted by smaller nanowires is observed, while 10.8 ± 1.5 at. % Ti leads to

DOI: 10.1021/acs.chemmater.6b02470
Chem. Mater. 2016, 28, 7666−7672

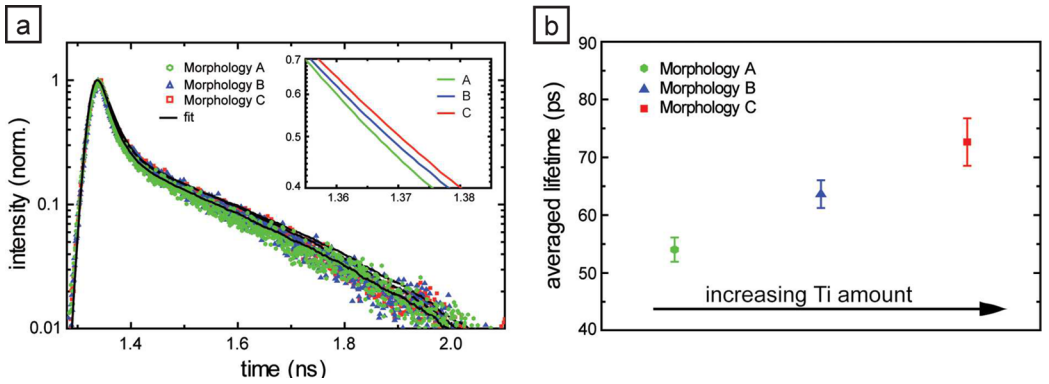

Figure 4. (a) Semi-log plot of TCSPC transients detected for the three different morphologies after pulsed two-photon excitation at 1.7 eV. The inset, a zoom-in of the biexponential fits of the PL decay dynamics, shows longer PL decay times for an increasing Ti amount incorporated in the superstructures. (b) Intensity-averaged lifetimes for the three different morphologies (for further details, see Figure S15 of the Supporting Information). An increase of the intensity-averaged lifetime can be observed with increasing the Ti amount in the material.

cubic superstructures built up from small nanoplates. The amount of titanium that can be incorporated into the crystal lattice is limited to around 12 at. %, with further titanium excess resulting in the formation of niobium-doped anatase TiO_2 plates. These TiO_2 plates grow on the surface of $Nb_3O_7(OH)$ nanowires which integrate into the anatase TiO_2 plate, via oriented crystal growth.

Morphologies formed in the presence of titanium show higher photocatalytic H_2 evolution rates than pristine $Nb_3O_7(OH)$ superstructures. PL lifetime measurements indicate a lower density of quenching sites at the surface of the crystals in the presence of titanium. This could be caused by a reduced amount of hydroxyl groups, which is required to achieve charge neutrality upon Ti doping. The substitution of Nb^{5+} by Ti^{4+} means that fewer hydroxyl groups are needed for charge balance $[Nb_{3-x}Ti_xO_7(OH)_{1-x}]$, which is indicated by enhanced PL lifetimes observed for morphologies B and C and a shift in the *d* spacings observed in the XRD pattern. For morphology B, no TiO_2 crystal phase was discovered, so that the doubled H_2 evolution rate observed for this morphology (1773 μmol h^{-1} g^{-1}) compared to pristine $Nb_3O_7(OH)$ superstructures (870 μmol h^{-1} g^{-1}) can be attributed to a combination of a reduced density of quenching sites near the surface and the increased surface area of morphology B. Morphology C is overgrown by TiO_2 plates, which form as a result of excess Ti(IV) in the reaction solution. However, the H_2 evolution rate observed for this morphology is only slightly higher than the H_2 evolution rate of morphology B, indicating that the presence of TiO_2 does not significantly enhance the photocatalytic activity.

Still, active band gap engineering is required to extend the optical absorption of $Nb_3O_7(OH)$ more toward the visible regime, which would yield higher efficiencies.

■ ASSOCIATED CONTENT

Supporting Information

The Supporting Information is available free of charge on the ACS Publications website at DOI: 10.1021/acs.chemmater.6b02470.

Materials and Methods section, EDX and ICP data for morphology B, SEM images of all three morphologies, XRD data, TEM data of all three morphologies, EELS data, fast Fourier transform (FFT) data, ultraviolet/visible (UV/vis) spectra for all three morphologies, H_2 production rate of morphology B, and PL data (PDF)

■ AUTHOR INFORMATION

Corresponding Author

*E-mail: c.scheu@mpie.de.

Notes

The authors declare no competing financial interest.

■ ACKNOWLEDGMENTS

The authors acknowledge Tina Reuther for support on the BET measurements, Christoph Heinzl for fruitful discussions and support on the TEM measurements, Jim Ciston, Karen Bustillo, Chengyu Song, Markus Döblinger, and Steffen Schmidt for technical support on TEM, Jaroslava Obel for the ICP measurements, and Prof. Thomas Bein, who granted access to the X-ray diffractometer and UV/vis spectrometer. Furthermore, financial support of the Center for NanoScience, the German Excellence Initiative of the Deutsche Forschungsgemeinschaft (DFG) via the "Nanosystems Initiative Munich (NIM)", is gratefully acknowledged. Work at the Molecular Foundry was supported by the Office of Science, Office of Basic Energy Sciences of the U.S. Department of Energy under Contract DE-AC02-05CH11231.

■ REFERENCES

(1) Ahmad, H.; Kamarudin, S. K.; Minggu, L. J.; Kassim, M. Hydrogen from photo-catalytic water splitting process: A review. *Renewable Sustainable Energy Rev.* **2015**, *43*, 599−610.

(2) Kudo, A.; Miseki, Y. Heterogeneous Photocatalyst Materials for Water Splitting. *Chem. Soc. Rev.* **2009**, *38*, 253−278.

(3) Chen, X.; Mao, S. Titanium Dioxide Nanomaterials: Synthesis, Properties, Modifications, and Applications. *Chem. Rev.* **2007**, *107*, 2891−2959.

(4) Weng, Z.; Guo, H.; Liu, X.; Wu, S.; Yeung, K.; Chu, P. Nanostructured TiO_2 for Energy Conversion and Storage. *RSC Adv.* **2013**, *3*, 24758−24775.

(5) Fujishima, A.; Honda, K. Electrochemical Photolysis of Water at a Semiconductor Electrode. *Nature* **1972**, *238*, 37−38.

(6) Ni, M.; Leung, M.; Leung, D.; Sumathy, K. A Review and Recent Developments in Photocatalytic Water-Splitting Using TiO_2 for Hydrogen Production. *Renewable Sustainable Energy Rev.* **2007**, *11*, 401−425.

(7) Wang, M.; Ioccozia, J.; Sun, L.; Lin, C.; Lin, Z. Inorganic-Modified Semiconductor TiO_2 Nanotube Arrays for Photocatalysis. *Energy Environ. Sci.* **2014**, *7*, 2182−2202.

DOI: 10.1021/acs.chemmater.6b02470
Chem. Mater. 2016, 28, 7666−7672

(8) O'Regan, B.; Grätzel, M. A. A Low-Cost, High-Efficiency Solar Cell Based on Dye-Sensitized Colloidal TiO_2 Films. *Nature* **1991**, *353*, 737−740.
(9) Snaith, H.; Schmidt-Mende, L. Advances in Liquid-Electrolyte and Solid-State Dye-Sensitized Solar Cells. *Adv. Mater.* **2007**, *19*, 3187−3200.
(10) Hagfeldt, A.; Boschloo, G.; Sun, L.; Kloo, L.; Pettersson, H. Dye-Sensitized Solar Cells. *Chem. Rev.* **2010**, *110*, 6595−6663.
(11) Sauvage, F.; Di Fonzo, F.; Li Bassi, A.; Casari, C.; Russo, V.; Divitini, G.; Ducati, C.; Bottani, C.; Comte, P.; Grätzel, M. Hierarchical TiO_2 Photoanode for Dye-Sensitized Solar Cells. *Nano Lett.* **2010**, *10*, 2562−2567.
(12) Osterloh, F. Inorganic Materials as Catalysts for Photochemical Splitting of Water. *Chem. Mater.* **2008**, *20*, 35−54.
(13) Hernández-Alonso, M.; Fresno, F.; Suárez, S.; Coronado, J. Development of Alternative Photocatalysts to TiO_2: Challenges and Opportunities. *Energy Environ. Sci.* **2009**, *2*, 1231−1257.
(14) Yang, L.; Zhou, H.; Fan, T.; Zhang, D. Semiconductor Photocatalysts for Water Oxidation: Current Status and Challenges. *Phys. Chem. Chem. Phys.* **2014**, *16*, 6810−6826.
(15) Hu, P.; Hou, D.; Shi, H.; Chen, C.; Huang, Y.; Hu, X. Microwave-assisted synthesis of self-assembled $BiO_{1.84}H_{0.08}$ hierarchical nanostructures as a new photocatalyst. *Appl. Surf. Sci.* **2014**, *319*, 244−249.
(16) Hu, P.; Hu, X.; Chen, C.; Hou, D.; Huang, Y. Biomaterial-assisted synthesis of AgCl@Ag concave cubes with efficient visible-light-driven photocatalytic activity. *CrystEngComm* **2014**, *16*, 649−653.
(17) Jose, R.; Thavasi, V.; Ramakrishna, S. Metal Oxides for Dye-Sensitized Solar Cells. *J. Am. Ceram. Soc.* **2009**, *92*, 289−301.
(18) Lin, H.-Y.; Yang, H.-C.; Wang, W.-L. Synthesis of Mesoporous Nb_2O_5 Photocatalysts with Pt, Au, Cu and NiO Cocatalyst for Water Splitting. *Catal. Today* **2011**, *174*, 106−113.
(19) Gao, B.; Fu, J.; Huo, K.; Zhang, W.; Xie, Y.; Chu, P. Quasi-Aligned Ag-Nb_2O_5 Nanobelt Arrays with Enhanced Photocatalytic and Antibacterial Activities. *J. Am. Ceram. Soc.* **2011**, *94*, 2330−2338.
(20) Zhang, H.; Wang, Y.; Yang, D.; Li, Y.; Liu, H.; Liu, P.; Wood, B.; Zhao, H. Directly Hydrothermal Growth of Single Crystal $Nb_3O_7(OH)$ Nanorod Film for High Performance Dye-Sensitized Solar Cells. *Adv. Mater.* **2012**, *24*, 1598−1603.
(21) Zhao, Y.; Zhou, X.; Ye, L.; Tsang, S. Nanostructured Nb_2O_5 Catalysts. *Nano Rev.* **2012**, *3*, 1−11.
(22) Li, L.; Deng, J.; Yu, R.; Chen, J.; Wang, Z.; Xing, X. Niobium Pentoxide Hollow Nanospheres with Enhanced Visible Light Photocatalytic Activity. *J. Mater. Chem. A* **2013**, *1*, 11894−11900.
(23) Luo, H.; Song, W.; Hoertz, P.; Hanson, K.; Ghosh, R.; Rangan, S.; Brennaman, M.; Concepcion, J.; Binstead, R.; Bartynski, R.; Lopez, R.; Meyer, T. A Sensitized Nb_2O_5 Photoanode for Hydrogen Production in a Dye-Sensitized Photoelectrosynthesis Cell. *Chem. Mater.* **2013**, *25*, 122−131.
(24) Betzler, S.; Wisnet, A.; Breitbach, B.; Mitterbauer, C.; Weickert, J.; Schmidt-Mende, L.; Scheu, C. Template-free Synthesis of Novel, Highly-Ordered 3D Hierarchical $Nb_3O_7(OH)$ Superstructures with Semiconductive and Photoactive Properties. *J. Mater. Chem. A* **2014**, *2*, 12005−12013.
(25) Hmadeh, M.; Hoepfner, V.; Larios, E.; Liao, K.; Jia, J.; Jose-Yacaman, M.; Ozin, G. New Hydrogen-Evolution Heteronanostructured Photocatalysts: Pt-$Nb_3O_7(OH)$ and Cu-$Nb_3O_7(OH)$. *ChemSusChem* **2014**, *7*, 2104−2109.
(26) Hu, P.; Hou, D.; Wen, Y.; Shan, B.; Chen, C.; Huang, Y.; Hu, X. Self-Assembled 3D Hierarchical Sheaf-Like $Nb_3O_7(OH)$ Nanostructures with Enhanced Photocatalytic Activity. *Nanoscale* **2015**, *7*, 1963−1969.
(27) Betzler, S.; Harzer, T.; Ciston, J.; Dahmen, U.; Dehm, G.; Scheu, C. Heat-Induced Phase Transformation of Three-Dimensional $Nb_3O_7(OH)$ Superstructure: Effect of Atmosphere and Electron Beam. *Cryst. Growth Des.* **2016**, *16*, 4309−4317.
(28) Khan, W.; Betzler, S.; Šipr, O.; Ciston, J.; Blaha, P.; Scheu, C.; Minar, J. Theoretical and Experimental Study on the Optoelectronic Properties of $Nb_3O_7(OH)$ and Nb_2O_5 Photoelectrodes. *J. Phys. Chem. C* **2016**, DOI: 10.1021/acs.jpcc.6b06391.
(29) Wu, J.; Wang, J.; Li, H.; Xue, D. Solution-Phase Tailored Growth of $Nb_3O_7(OH)$ Thin Films. *Thin Solid Films* **2013**, *544*, 545−550.
(30) Agarwal, G.; Reddy, G. Study of Surface Morphology and Optical Properties of Nb_2O_5 Thin Films with Annealing. *J. Mater. Sci.: Mater. Electron.* **2005**, *16*, 21−24.
(31) Wisnet, A.; Bader, K.; Betzler, S.; Handloser, M.; Ehrenreich, P.; Pfadler, T.; Weickert, J.; Hartschuh, A.; Schmidt-Mende, L.; Scheu, C.; Dorman, J. Defeating Loss Mechanisms in 1D TiO_2-Based Hybrid Solar Cells. *Adv. Funct. Mater.* **2015**, *25*, 2601−2608.
(32) Izumi, F.; Kodama, H. Hydrothermal Synthesis and Characterization of $Nb_3O_7(OH)$. *Z. Anorg. Allg. Chem.* **1978**, *441*, 196−204.
(33) Zhang, F.; Chan, S.-W.; Spanier, J.; Apak, E.; Jin, Q.; Robinson, R.; Herman, I. Cerium Oxide Nanoparticles: Size-Selective Formation and Structure Analysis. *Appl. Phys. Lett.* **2002**, *80*, 127−129.
(34) Shannon, R. Revised Effective Ionic Radii and Systematic Studies of Interatomic Distances in Halides and Chalcogenides. *Acta Crystallogr., Sect. A: Cryst. Phys., Diffr., Theor. Gen. Crystallogr.* **1976**, *32*, 751−767.
(35) Bach, D.; Schneider, R.; Gerthsen, D.; Verbeeck, J.; Sigle, W. EELS of Niobium and Stoichiometric Niobium-Oxide Phases-Part I: Plasmon and Near-Edges Fine Structure. *Microsc. Microanal.* **2009**, *15*, 505−523.
(36) Brydson, R.; Sauer, H.; Engel, W.; Thomass, J.; Zeitler, E.; Kosugi, N.; Kuroda, H. Electron Energy Loss and X-ray Spectroscopy of Rutile and Anatase: A Test of Structural Sensitivity. *J. Phys.: Condens. Matter* **1989**, *1*, 797−812.
(37) Stoyanov, E.; Langenhorst, F.; Steinle-Neumann, G. The Effect of Valence State and Site Geometry on Ti-$L_{2,3}$ and O-K Electron Energy-Loss Spectra of Ti_xO_y Phases. *Am. Mineral.* **2007**, *92*, 577−586.
(38) Sasikala, R.; Sudarsan, V.; Sudakar, C.; Naik, R.; Panicker, L.; Bharadwaj, S. R. Modification of the Photocatalytic Properties of Self Doped TiO_2 Nanoparticles for Hydrogen Generation Using Sunlight Type Radiation. *Int. J. Hydrogen Energy* **2009**, *34*, 6105−6113.
(39) Gokus, T.; Hartschuh, A.; Harutyunyan, H.; Allegrini, M.; Hennrich, F.; Kappes, M.; Green, A.; Hersam, M.; Araújo, P.; Jorio, A. Exciton Decay Dynamics in Individual Carbon Nanotubes at Room Temperature. *Appl. Phys. Lett.* **2008**, *92*, 153116−3.
(40) Zhou, H.; Alves, H.; Hofmann, D.; Kriegseis, W.; Meyer, B.; Kaczmarczyk, G.; Hoffmann, A. Behind the Weak Excitonic Emission of ZnO Quantum Dots: ZnO/Zn(OH) Core-Shell Structure. *Appl. Phys. Lett.* **2002**, *80*, 210−212.
(41) Xiong, G.; Pal, U.; Serrano, J. Correlations Among Size, Defects, and Photoluminescence in ZnO Nanoparticles. *J. Appl. Phys.* **2007**, *101*, 024317−6.

DOI: 10.1021/acs.chemmater.6b02470
Chem. Mater. 2016, 28, 7666−7672